JGR Solid Earth

RESEARCH ARTICLE
10.1029/2019JB018141

# Physically Consistent Modeling of Dike-Induced Deformation and Seismicity: Application to the 2014 Bárðarbunga Dike, Iceland

**Elías R. Heimisson**[1,2] **and Paul Segall**[1]

[1]Department of Geophysics, Stanford University, Stanford, CA, USA, [2]Now at Seismological Laboratory, California Institute of Technology, Pasadena, CA, USA

**Key Points:**
- The model captures the complex space-time history of seismicity and deformation
- Results are consistent with dike-induced earthquakes being triggered on preexisting faults
- Magma pressure increases when the dike stops but drops rapidly as it propagates

**Supporting Information:**
- Supporting Information S1
- Movie S1

**Correspondence to:**
E. R. Heimisson,
eliasrh@stanford.edu;
eheimiss@caltech.edu

**Citation:**
Heimisson, E. R., & Segall, P. (2020). Physically consistent modeling of dike-induced deformation and seismicity: Application to the 2014 Bàrðarbunga dike, Iceland. *Journal of Geophysical Research: Solid Earth*, *125*, e2019JB018141. https://doi.org/10.1029/2019JB018141

Received 1 JUN 2019
Accepted 22 JAN 2020
Accepted article online 26 JAN 2020



**Abstract** Dike intrusions are often associated with surface deformation and propagating swarms of earthquakes. These are understood to be manifestations of the same underlying physical process, although rarely modeled as such. We construct a physics-based model of the 2014 Bárðarbunga dike, by far the best observed large dike (>0.5 km$^3$) to date. We constrain the background stress state by the total dike deformation, the time-dependent dike pressure from continuous GPS and the extent of the seismic swarm, and the spatial dependence of frictional properties via the space-time evolution of seismicity. We find that the geodetic and earthquake data can be reconciled with a self-consistent set of parameters. The complex spatial and temporal evolution of the Bárðarbunga seismicity can be explained by dike-induced elastic stress changes on preexisting faults, constrained by observed focal mechanisms. In particular, the model captures the segmentation of seismicity, where only the newest dike segment is seismically active. Our results indicate that many features of the seismicity result from the interplay between time-dependent magma pressure within the dike and stress memory effects. The spatial variability in seismicity requires heterogeneity in frictional properties and/or local initial stresses. Modeling suggests that the dike pressure drops during rapid advances and increases during pauses, which primarily causes the segmentation of the seismicity. Joint analysis of multiple data types could potentially lead to improved, physics-based eruption forecasts.

## 1. Introduction

A propagating dike deforms the crust and causes dramatic stress changes in the near field; this usually results in a propagating swarm of seismicity. It is generally thought that the leading edge of the seismicity marks the approximate location of the dike tip since that is where the local stresses are largest. The September 1977 Krafla, Iceland, dike intrusion provides convincing evidence for seismicity being produced near the dike tip. Dike propagation was marked by a swarm of seismicity that migrated ~8 km from the center of the Krafla caldera, eventually intersecting a geothermal well (Brandsdottir & Einarsson, 1979). A small volume of basaltic tephra erupted from the borehole (Larsen & Grönvold, 1979), shortly after the earthquakes propagated into the vicinity of the well. Despite this clear association, the exact mechanism of dike-induced seismicity is not completely understood.

Seismicity and deformation have long been successfully used to study, and even forecast, volcanic processes. Yet, most studies do not jointly model the two types of data quantitatively, although they are usually considered signatures of the same underlying process. Modeling deformation in volcanic settings is reasonably well understood on short time scales when elastic deformation predominates. However, modeling earthquake production or seismicity rate in response to stress changes is currently a subject of active research. Here we investigate seismicity triggered by a propagating dike into a critically stressed and faulted rift zone. We thus expect that seismicity should manifest as slip on preexisting faults, which can be described by a rate-and-state-based seismicity model law (Segall et al., 2013). This approach contrasts with models that describe damage accumulation in formerly unfaulted crust (e.g., Got et al., 2017). To gain further insight into dynamic, and sometimes life-threatening, Earth processes we seek to develop quantitative models that are consistent with more than one independent data type. The goal of this study is to develop such a model and apply it to the 2014 Bárðarbunga dike intrusion, with fully consistent deformation and stress fields that affect GPS, Interferometric Synthetic Aperture Radar (InSAR), and seismicity data. Such a framework could potentially lead to improved, physics-based eruption forecasts.

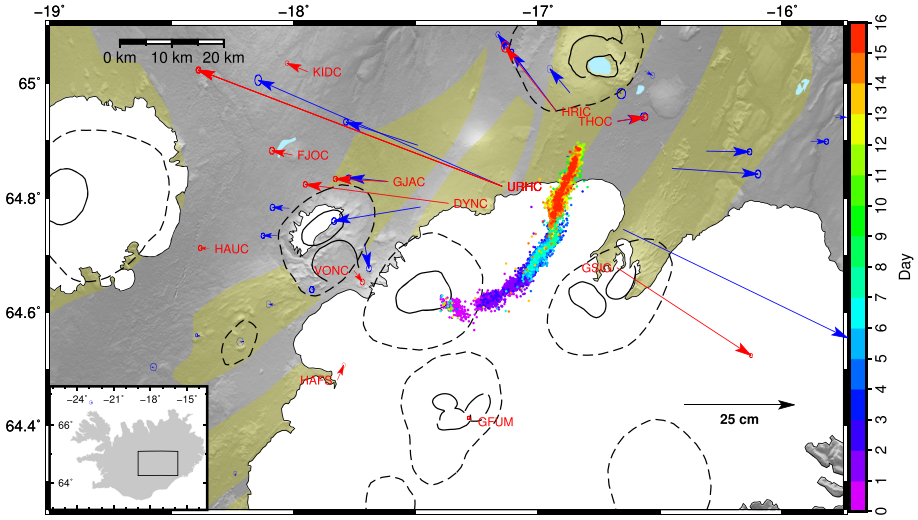


**Figure 1.** Location of the Bárðarbunga volcano, dike seismicity, and net GPS displacements. Dashed lines mark individual central volcanoes, solid lines are caldera faults, and yellow shaded areas are fissure swarms associated with central volcanoes. Vectors show cumulative displacement spanning the 2014 diking event. Red arrows, and labels, are continuous GPS stations used in the time-dependent inversion. Blue arrows are campaign GPS stations. Dots show dike seismicity from Ágústsdóttir et al. (2019), which are color coded by days since the beginning of the intrusion.

Most studies of dike-induced deformation apply kinematic dislocation models (e.g., Du & Aydin, 1992; Green et al., 2015; Jónsson et al., 1999; Sigmundsson et al., 2015). These models are subject to ad hoc regularization to smooth the dike opening, where the degree of smoothing is based on signal-to-noise ratio of the data, not the physics of pressurized cracks. A different approach to modeling magmatic intrusions is to derive opening from traction boundary conditions (e.g., Cayol & Cornet, 1998; Hooper et al., 2011; Segall et al., 2013; Sigmundsson et al., 2010; Yun et al., 2006). We refer to this as a magmastatic crack model since viscous stresses acting on the dike walls are neglected. This approach greatly reduces the number of free parameters and results in a smoothly varying opening corresponding to a fluid-filled crack in static equilibrium with the crustal stress state. An important benefit of this approach is that it yields more realistic stress fields surrounding the dike, whereas kinematic dislocation models fail to accurately represent the near field stresses imposed by the dike.

Our study may be regarded as a test of the hypothesis that a physics-based dike model, constrained by geodetic observations, can be reconciled with the complex spatial and temporal evolution of seismicity during the 2014 Bárðarbunga dike intrusion using an earthquake production law based on rate-and-state friction (Dieterich, 1994; Heimisson & Segall, 2018). Specifically, we hypothesize that seismicity is triggered on prestressed faults that host a population of seismic sources with heterogeneous initial conditions. Our findings suggest that these models are in general agreement with observations.

Segall et al. (2013) took the first step toward a joint quantitative analysis of microseismicity and surface deformation during dike propagation. They performed a joint inversion of data from the 2007 “Father's Day” intrusion in Kilauea. Using a boundary element crack model, they related dike opening to surface displacements and changes in stresses in volume elements (voxels) surrounding the dike. From the predicted shear and normal tractions, acting on fault planes inside each voxel, the cumulative number of events was computed using the Dieterich (1994) seismicity rate theory. In a broad sense, we apply the same approach to the Bárðarbunga dike; however, the Bárðarbunga dike was much larger and better monitored than Father's Day intrusion, with a more complicated spatial and temporal evolution. This resulted in a much richer and more complete data set. For example, the Bárðarbunga dike was monitored by nearly a dozen continuous GPS stations (Figure 1), InSAR acquisitions, and a dense seismic network, which was used to locate over 30,000 events with high accuracy (Ágústsdóttir et al., 2016). In contrast, the Father's Day intrusion only had a few hundred located events. Because of the nonplanar geometry of the Bárðarbunga dike we discretize the surrounding crust into tetrahedral voxels. Furthermore, we allow the dike to evolve vertically, as well as laterally, in a realistic tectonic stress field; in contrast, the height of the Fathers Day dike was fixed.

In section 2, we discuss how we construct the dike model, and the numerical strategy for computing the dike opening and model-predicted seismicity. In section 3, we discuss a three-step inversion strategy and show the results of each step: First, we constrain the crustal and magma densities and background stress field surrounding the dike using cumulative GPS and InSAR displacements. Second, we constrain the time-dependent pressure in the dike using continuous GPS data. Third, we constrain parameters related to the earthquake production law and simulate the earthquake catalog. Section 4 offers a discussion of the results and model assumptions and explains interesting phenomena observed in the seismicity.

### 1.1. The 2014 Bárðarbunga Dike, Iceland

The 2014 Bárðarbunga dike is by far the best instrumented large dike intrusion to date, with more than 30,000 detected earthquakes (Ágústsdóttir et al., 2016). Large deformations were observed by continuous GPS and a number of InSAR acquisitions (Sigmundsson et al., 2015). The high-quality data led to the following observations: The seismicity was mostly concentrated in a limited depth range of 5–7 km, and segmented along strike, with only the newest dike segment seismically active (Ágústsdóttir et al., 2016) (Figure 1). In this paper we use the word *segmentation* in the same sense as Sigmundsson et al. (2015). The trajectory of the dike had several abrupt turns; propagation often halted before changing direction. Continuous GPS data show that the dike inflated during these pauses implying it accumulated magma (Sigmundsson et al., 2015).

The initial analysis of seismicity (Sigmundsson et al., 2015) revealed some variability in focal mechanisms among the larger events, ranging from strike slip to normal; most estimated focal mechanisms were significantly oblique. A later study by Ágústsdóttir et al. (2016) investigated focal mechanisms at the distal end (the last ~13 km) of the dike with a much denser network. They found the dominant focal mechanism (85% of analyzed events) to be strike slip with the same strike and no significant volumetric component. Based on which nodal plane was better constrained by the data and the orientation of the regional stress field, they concluded that these are left-lateral events with strike 38° east of north. The dike in this region strikes 25°. The other common focal mechanisms in this region are right-lateral slip with a strike of ~17°. These mechanisms tend to occur only behind the leading edge of the dike. Along the first 0–10 km of the dike the mechanisms are highly variable. From 10–30 km, the mechanisms appear to have similar strike as the end region (~38°) but are predominantly right lateral. From 30 km to the end region the events are predominantly left lateral (see Ágústsdóttir et al., 2019, for details). We apply these inferred fault planes as prior constraints, as detailed in section 3.3.

Green et al. (2015), Parks et al. (2017), Ruch et al. (2016), and Sigmundsson et al. (2015) previously modeled the surface deformation due to the dike and the Bárðarbunga caldera collapse. However, most of the published studies have employed kinematic dislocation models. In contrast, in this study, we try to model realistic near-field stresses. This is required to capture the temporally complex propagation of seismicity (Figure 1), and to accurately predict the cumulative number of earthquakes. In the following section, we describe the dike model in detail, along with a description of its limitations.

## 2. Methods

### 2.1. Dike Model

Dike opening is controlled by the difference between the dike normal stress $\sigma = P_{litho} + \sigma_n$ and the magma pressure $P$; the dike overpressure is $\Delta P = P - \sigma = P - (P_{litho} + \sigma_n)$ (Figures 2a and 2b). Here, $P_{litho}$ is the lithostatic pressure and $\sigma_n$ is the component of the tectonic stress field normal to the dike. The density of the crust varies with depth, and at shallow levels is typically less than the density of basaltic magma. The density contrast can stabilize the dike vertically and promote lateral propagation (e.g., Fialko & Rubin, 1999; Townsend et al., 2017). The depth where the density of the magma and crust is the same is referred to as the level of neutral buoyancy (LNB). This may not be where the maximum opening occurs, since that also depends on $\sigma_n$.

Near the top and bottom boundary of the dike the overpressure may change sign even though the dike opening is nonnegative. Furthermore, at the laterally propagating dike tip (Figure 2c) there is likely a magma-free cavity filled with pore fluids from the crust or exsolved volatiles from the magma (Rubin, 1993). The pressure inside the cavity is highly uncertain, but one end member case is that the cavity pressure is negligible such that the overpressure there is $\Delta P \sim -\sigma$; this is assumed here (note $\Delta P < 0$ is an *underpressure*). The length of the tip cavity can be solved for under the assumption that the crack is nonsingular, as described

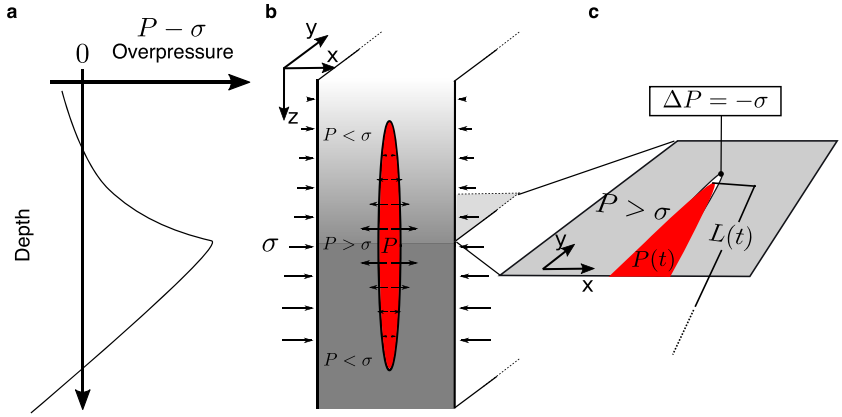


**Figure 2.** Schematic cross section showing the depth dependent parameters that affect dike opening. (a) Schematic overpressure profile within a vertical dike cross section. (b) Schematic dike opening with both top and bottom tip underpressured. The opening is drawn as elliptical, although that is not consistent with the overpressure profile. (c) Dike tip at the lateral end with a crack tip cavity and length $L(t)$ defined as the distance to the front of the pressurized magma.

later. A cavity may exist at the top and bottom margins (Figure 2b) but the depth dependence of $P-\sigma$ results in a more gradual transition where the over pressure becomes negative, resulting in a nonsingular crack tip without introducing a tip cavity (Figure 2a).

To attain realistic stresses in the near field, we simulate a nonsingular crack. It is fairly straightforward to compute the size of the crack tip cavity for a simple 1-D geometry given a specified pressure distribution (e.g., Fialko & Rubin, 1999). However, this is less obvious when the crack is 2-D and pressure boundary conditions are spatially variable. We developed a method that achieves this for arbitrary dike pressure and geometry. The process is iterative and is loosely based on simulating the fracture process during an intrusion. One starts by setting up a grid of dislocation elements that cover the dike surface. The iterative approach can then be described in the following steps:

1. Select dislocations elements where magma is located and the dike walls subject to positive overpressure. This represents the initial singular crack.
2. Use the boundary element approach (described below) to solve for the dike opening.
3. Compute normal tractions on the rest of the grid due to both dike opening and the resolved background stress.
4. Find elements subject to less compression than the predefined crack underpressure at that location. If there are no such elements the stress singularity has been canceled to the resolution of the grid, otherwise continue to the next step.
5. Assign the specified underpressure to these elements and move to step 2.

The vertical distribution of overpressure is parameterized by a single value of magma pressure at the LNB $P(z_{LNB})$, where the crustal density is the same as the magma density. The dike overpressure $\Delta P(z)$ along a vertical cross section is

$$\Delta P(z) = \rho_m g(z - z_{LNB}) + P(z_{LNB}) - \sigma(z), \tag{1}$$

where $z$ is depth, $\rho_m$ is magma density, and $\sigma = \sigma^T_{ij} v_i v_j + P_{litho}(z)$ is the dike normal traction ($v_i$ is the dike plane normal vector; thus, $\sigma_n = \sigma^T_{ij} v_i v_j$) due to the stress tensor $\sigma^T_{ij}$ derived from tectonic loading and $P_{litho}$, the lithostatic pressure. The latter is computed from the density of the Icelandic crust from Guðmundsson and Högnadóttir (2007), based on data from Carlson and Herrick (1990) and Christensen and Wilkens (1982). The tectonic stress is computed from a (tapered) buried opening dislocation to model deep rifting and plate spreading. The opening is tapered using a segment of a fourth-order polynomial with zero slopes at both ends to attain nonsingular stresses (see section 3.1.1 for details).

The lateral extent of dike overpressure is indicated by the parameter $L$ that controls the dike length along strike. We assume that between 0 and $L$ that $P(z_{LNB})$ is spatially constant at any given time. Crack opening beyond $L$ is found by computing the size of the dike tip cavity that cancels the stress singularity. The initial

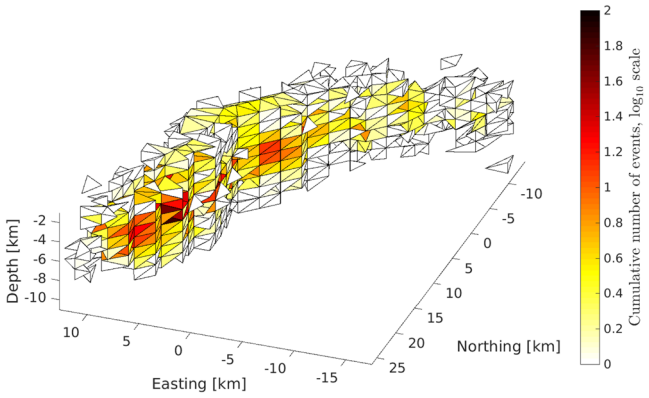


**Figure 3.** Total number of earthquakes in each voxel, binned into a mesh of voxels with mean edge length of 1.5 km.

crack for the algorithm, described above, is taken as the region where $\Delta P > 0$ for all dislocations within distance $L$ along the dike plane. Thus, $L$ does not represent the fracture length, which varies with depth, but the length where $\Delta P > 0$ at $z = z_{LNB}$.

### 2.2. Boundary Element Implementation

The surface in which the dike can propagate is fixed based on seismicity and has fixed dislocation element discretization. This is different from the approach of Segall et al. (2013), where the discretization of the dike evolved as the dike propagated. The latter approach allows the dike length $L(t)$ to be a continuous variable. In contrast, the approach here renders $L(t)$ discrete, for computational efficiency admissible lengths are predefined by the initial discretization of the dike. This, in turn, results in an objective function that is a discrete function of $L$, precluding gradient-based optimization methods. In spite of this, there are significant advantages in terms of computational efficiency since repeated calculations of the Green's functions are avoided.

Consider the matrix of influence coefficients $\boldsymbol{G}$ that relates a vector of opening $\boldsymbol{b}$ to the vector of overpressure acting on each dislocation element $\boldsymbol{\Delta P}$ in an elastic half-space:

$$\boldsymbol{\Delta P} = \boldsymbol{G}\boldsymbol{b} \Rightarrow \boldsymbol{b} = \boldsymbol{G}^{-1}\boldsymbol{\Delta P}. \tag{2}$$

Computing $\boldsymbol{G}$ is computationally expensive. For $n$ opening mode dislocations, $\boldsymbol{G}$ has $n^2$ elements. If the crack geometry changes then all or a part of $\boldsymbol{G}$ changes, such that in a time-dependent inversion $\boldsymbol{G}$ typically changes in every iteration. That is the approach taken by Segall et al. (2013); however, since they assumed a planar dike, they could use translational symmetry to reduce the number of function calls. The 2014 Bárðarbunga dike is not planar, which means that such symmetries do not exist. We, therefore, compute $\boldsymbol{G}$ only once for a fixed grid and store the matrix. The algorithm outlined in section 2.1 is then used to select dislocation elements that contribute to the opening of the dike. The rows and columns of $\boldsymbol{G}$ corresponding to elements outside the periphery of the dike, including the tip cavity, are removed before the matrix is inverted to solve for the vector of opening $\boldsymbol{b}$.

Ruch et al. (2016) showed that a small amount of strike slip occurred on faults parallel to the dike and other deformation studies have also suggested that some slip occurred on the dike plane (Sigmundsson et al., 2015; Spaans & Hooper, 2018). Here we neglect this for two reasons. First, the dominant displacement across the dike is opening; thus, the contribution from strike-slip displacements to the deformation and stresses will be secondary. Second, including a strike-slip contribution in $\boldsymbol{G}$ renders the matrix four times as large. This poses computational problems since the matrix is already very large and nonsparse.

### 2.3. Modeling the Seismicity Rate

Due to the kinked path of the Bárðarbunga dike, we cannot use the same approach as Segall et al. (2013) where the seismicity rate is computed in rectangular voxels. In order to best utilize the seismicity data, we form a mesh of tetrahedra elements surrounding the dike (Figure 3). The tetrahedral mesh is chosen such that voxels do not cross the dike plane. Dislocations have stress singularities that are proportional to the opening, or if dislocations align in the same plane, to the difference in opening of two adjacent dislocations. Thus, a smoothly varying opening will greatly decrease the influence of these singularities. However, if the voxels intersect the dike plane stresses may be evaluated too close to a dislocation edge producing unrealistic values. We evaluate the stress tensor at Gauss points in each tetrahedron. Gaussian quadrature only uses points in the interior of the integration domain; this further limits the influence of singular stresses. An efficient way to mesh and guarantee that voxels do not cross the dike plane is to use Delaunay triangulation. It has the property that nearest neighbor points form an edge of the same triangle. Thus, by making sure any point on the dike plane also has the nearest neighbor on the dike plane, then the voxels will not intersect the plane of the dike (Figure 3). The stress tensor evaluated at Gauss points is then projected into normal and shear tractions acting on fault planes consistent with observed focal mechanisms.

We compute the cumulative number of earthquakes $N$ using the modified Dieterich 1994 theory of Heimisson and Segall (2018):

$$\frac{N}{r} = \frac{A\sigma_0}{\dot{s}_b} \log\left(\frac{\dot{s}_b}{A\sigma_0}\int_0^t K(t')dt' + 1\right), \tag{3}$$

where $r$ is the background rate of seismicity for a population, which we define for each voxel. $A$ is a constitutive parameter related to the direct effect in the rate-and-state friction law and relates changes in slip rate to friction. $\tau_0$ and $\sigma_0$ are the initial shear and normal stresses acting on the fault and $\dot{s}_b$ is the background Coulomb stressing rate where the coefficient of friction is $\mu = \tau_0/\sigma_0 - \alpha$. Here, $\alpha$ is a constant relating changes in normal stress to changes in state (Linker & Dieterich, 1992). The characteristic decay time of seismicity is $t_a = A\sigma_0/\dot{s}_b$. Time-dependent stress changes due to the intrusion are accounted for in the kernel $K(t)$:

$$K(t) = \exp\left(\frac{\tau(t)}{A\sigma(t)} - \frac{\tau_0}{A\sigma_0}\right)\left(\frac{\sigma(t)}{\sigma_0}\right)^{\alpha/A}, \tag{4}$$

where $\tau(t)$ and $\sigma(t)$ are the total shear and effective normal stress acting on the fault planes, respectively.

We apply the trapezoidal rule to the integral (3) in each voxel to estimate the scaled cumulative number of earthquakes $\tilde{\mathrm{N}} = N/r$ at time $t_i$ (where $t_1 = 0$). In the $m$th Gauss point in the $n$th voxel the approximation of equation (3) is

$$\tilde{\mathrm{N}}^{n,m}(t_i) = \frac{A^n\sigma_0^{n,m}}{\dot{s}_b^{n,m}} \log\left(\frac{\dot{s}_b^{n,m}}{A^n\sigma_0^{n,m}}\sum_{j=1}^{j=i}\frac{1}{2}(K^{n,m}(t_j) + K^{n,m}(t_{j+1}))(t_{j+1} - t_j) + 1\right), \tag{5}$$

where $\dot{s}_b^{n,m} = \dot{\tau}_b^{n,m} - (\tau_0^{n,m}/\sigma_0^{n,m} - \alpha^n)\dot{\sigma}_b^{n,m}$ is the background Coulomb stressing rate at Gauss point $m$ in voxel $n$. The kernel can be written in the same notation

$$K^{n,m}(t_j) = \exp\left(\frac{\tau^{n,m}(t_j)}{A^n\sigma^{n,m}(t_j)} - \frac{\tau^{n,m}(t_1)}{A^n\sigma^{n,m}(t_1)}\right)\left(\frac{\sigma(t)^{n,m}}{\sigma(t_1)^{n,m}}\right)^{\alpha^n/A^n}. \tag{6}$$

For further discussion on the meaning of various parameters and the derivation of equations (3) and (4), we refer the reader to Heimisson and Segall (2018).

We estimate the total number of predicted events in the $n$th voxel $N^n$ based on the scaled number events at the $m$ Gauss points:

$$\tilde{\mathrm{N}}^n(t_i) = r^n \frac{\sum_m w_{(n,m)}\tilde{\mathrm{N}}^{(n,m)}(t_i)}{\sum_m w_{(n,m)}}, \tag{7}$$

where $w_{(n,m)}$ are the Gauss weights of point $m$ in voxel $n$ and $r^n$ is the background rate of seismicity per unit volume of the $n$th voxel.

Equation (4) depends on the absolute shear and normal stress acting on a fault plane. The initial shear stress $\tau_0$ is the component of the traction vector for a given fault orientation parallel to the slip vector and computed directly from the dislocation model of the plate boundary, discussed in section 3.1.1, and $\Delta\tau(t)$ is the stress change due to dike opening. These two form the total shear stress: $\tau(t) = \tau_0 + \Delta\tau(t)$.

The effective normal stress acting on a population of seismic sources $\sigma(t)$ is a combination of several factors,

$$\sigma(t) = \sigma_0 + \Delta\sigma(t), \quad \text{where} \quad \sigma_0 = P_{litho} - \rho_w g z + \sigma_n \tag{8}$$

where $P_{litho}$ is the lithostatic pressure estimated from the density structure in Iceland (Guðmundsson & Högnadóttir, 2007), $\rho_w = 1{,}000$ kg/m$^3$ is the density of water, and $z$ the depth below the Earth's surface. The $\sigma_n$ is the normal component of the traction acting on the fault plane due to plate spreading, and $\Delta\sigma(t)$ is the time-dependent normal stress induced by the dike opening. In this paper we use the same notation for stresses acting on the dike plane and the fault planes, for example, $\sigma(t)$ in both cases reflects the total normal stress. This is done to emphasis that the dike and faults as subject to the ambient stress field and are physically consistent.

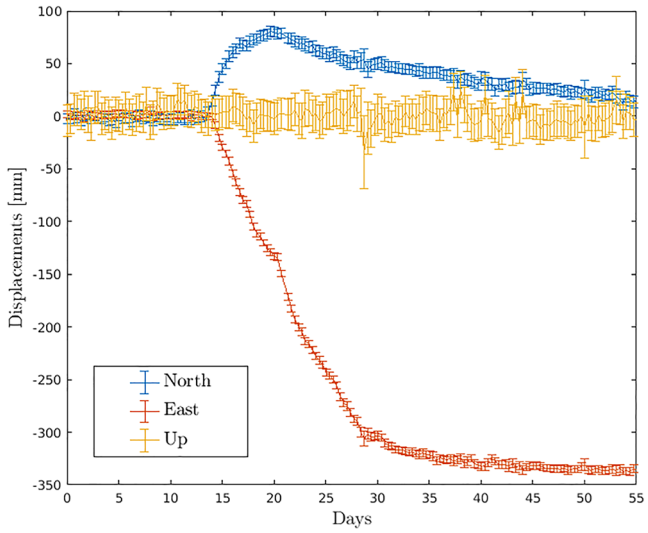


**Figure 4.** Eight hour time series at station DYNC shown as days since 1 August 2014. Dike starts propagating at around Day 15. Location of DYNC is shown in Figure 1.

### 2.4. Treatment of Observations

To determine the cumulative number of events, we first assign each earthquake to a voxel. We use the catalog of Ágústsdóttir et al. (2019) and magnitude estimates from Greenfield et al. (2018) and filter the catalog for the estimated magnitude of completeness of $M_c = 1$. Events not inside any voxel (about 2%) are excluded. The total time history $N(t)$ is interpolated using a piecewise cubic Hermite interpolating polynomial; then the interpolant is evaluated at predefined time steps. This interpolation scheme is shape preserving with continuous first derivative, which guarantees a nonnegative seismicity rate. To account for hypocentral errors, event locations are randomly perturbed within the estimated error bounds from Ágústsdóttir et al. (2019). The events are thus assigned multiple times to voxels; the mean number of earthquakes at time step $i$ in the $n$th voxel is taken to be $N_i^n$ and the standard deviation is $\sigma_i^n$, which are used in section 3.3.

We estimate that 100 time steps over a period of 16 days (during which the dike propagated and subsequently erupted) are needed to resolve first-order time-dependent features in the seismicity. To determine the cumulative GPS displacements at these 100 time steps, we interpolate the 8 hr time series (Figure 4) using a piecewise linear interpolation. The interpolation corresponds to upsampling the GPS time series by approximately a factor of 2.

## 3. Inversion

The model of the dike opening developed in section 2.1 is a function of the tectonic stress field, the lithostatic pressure gradient, the excess magma pressure and the magma density itself. All these fields influence the traction boundary conditions on the dike surface. We constrain parameters that control these fields with deformation data (section 3.1); this will be referred to as the *stress model*. Since these stresses do not change with time (except the magma pressure), we use InSAR and GPS data spanning the full intrusion (data from Sigmundsson et al., 2015) to estimate the time-independent fields. Next we estimate the time-dependent dike length and pressure using the continuous GPS time series; the resulting time-dependent model of dike opening will be referred to as the *dike model*. Finally, frictional and seismicity rate parameters are estimated from a temporal inversion of the number of earthquakes; given the dike model, this will be referred to as the *seismicity model* (section 3.3). In each step, the results of the previous estimations are used as constraints so that self-consistency is maintained.

### 3.1. Constraining the Background Stress Field

#### 3.1.1. Stress Model Setup

In this section we describe the stress model and set constraints for optimization based on a priori information.

Plate boundary deformation in the rift zones of Iceland has previously been modeled using buried dislocations (Árnadóttir et al., 2006; LaFemina et al., 2005). This assumes a constant rate of plate spreading below

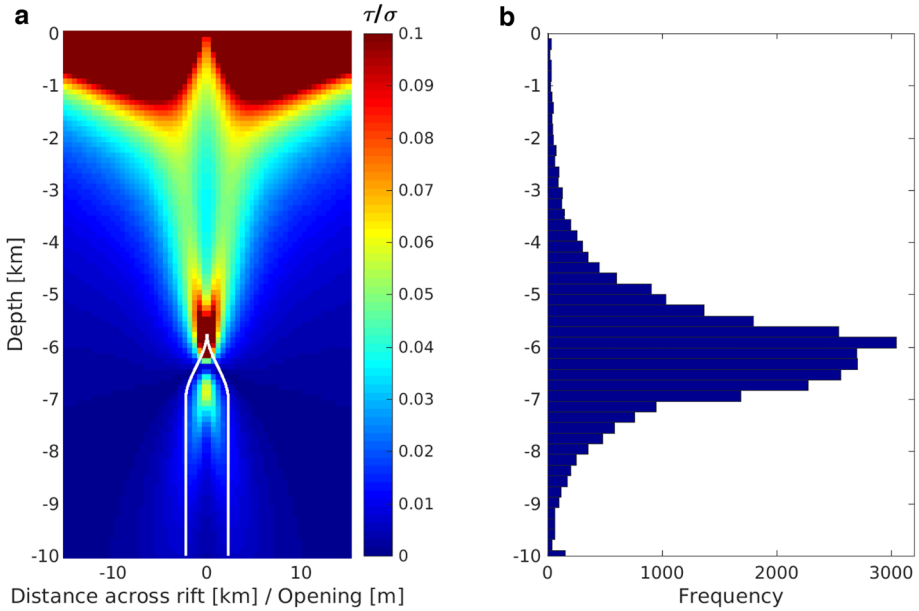


**Figure 5.** Depth-dependent stress predicted by a tapered buried dislocation. (a) ratio of horizontal shear stress to normal stress assuming lithostatic minus hydrostatic pressure gradient of $g{\cdot}1{,}750$ kg/m$^3$ with depth, with shear stress computed on a plane striking 15° east of the rift axis. Modified buried dislocation opening is shown with white lines with $l_b = 7$ km, cumulative opening of 4.5 m and tapers to 0 at $l_u = 5.75$ km depth. (b) histogram of earthquakes with depth located by Ágústsdóttir et al. (2016). High ratios of $\tau/\sigma$ promote higher rates of seismicity.

the brittle-ductile boundary under the central axis of the rift. This is represented as an infinitely deep vertical opening dislocation. The buried dislocation model is a highly idealized, yet has been shown to satisfy surface deformation data reasonably well in multiple tectonic settings (Árnadóttir et al., 2006; Hsu et al., 2003; LaFemina et al., 2005; Savage & Burford, 1973). It is thus a reasonable first-order model to capture tectonic stresses that build up between diking events.

To eliminate the stress singularity at the edge of the buried dislocation, we taper the opening such that the opening gradient goes to 0 at the topmost edge $l_u$, while at depth $l_b$ the opening reaches the full far-field extension rate. Thus, $l_b$ correspond crudely to the brittle-ductile boundary, where little stress from tectonic loading accumulates (Figure 5). This results in nonsingular stresses at $l_b$ and $l_u$.

In 1797 a dike propagated from Bárðarbunga and erupted in the Holuhraun area. The 2014 Bárðarbunga dike reoccupied the same crater row produced in 1797 (Hartley & Thordarson, 2013; Sigmundsson et al., 2015). Over the 217 year time span between eruptions, the cumulative opening deficit within the shallow rift zone due to plate motion is ~4 m, given an extension rate of 17.4 mm/yr (Drouin et al., 2017). Extension over the graben formed by the 2014 Bárðarbunga dike was in fact around 4.5 m (Ruch et al., 2016). We thus constrain the opening of the buried dislocation to be in the range 4.0–5.0 m. The rift axis strikes ~13.30–15.85° (Heimisson et al., 2015a), with its center under the Askja volcanic system north of the 2014 eruption (Sturkell & Sigmundsson, 2000). The depth to the brittle-ductile boundary is thought to be 6 to 8 km (Key et al., 2011; Soosalu et al., 2010), based on the depths of earthquakes. However, from fitting a buried dislocation to the plate boundary deformation in the Eastern Volcanic Zone in Iceland, LaFemina et al. (2005) found a best fitting depth of 13 km, although elastic buried dislocation models ignore possible viscoelastic effects, which may bias the depth. Most earthquakes during the 2014 dike intrusion were between 6 and 8 km depth, which suggests that 8 km is a lower limit to a range from 8 to 13 km depth for $l_b$. We keep the difference $l_b - l_u = 0.5$ km, constant in the inversion described later.

The density structure plays an important role in determining the lithostatic stress. Here, we use estimates from Guðmundsson and Högnadóttir (2007) and consider the density to increase linearly to depth $d_t$ of 4–6 km. Below $d_t$ the density is considered constant. We parameterize this density profile through two parameters: $\rho_1$ = 2,200–2,400 kg/m$^3$ (shallow crust), $\rho_2$ = 2,850–3,000 kg/m$^3$ (density at $d_t$ and below). Typical laboratory measurements of liquid basalt exhibit a range of densities of 2,650–2,800 kg/m$^3$

**Table 1**
*Summary of Parameters and Estimated Ranges for the Stress Model*

| Symbol | Description | Range | Optimal value |
|---|---|---|---|
| *Density structure* | | | |
| $d_t$ | Depth of density gradient changes | 4–6 km | 4.3 km |
| $\rho_1$ | Near surface density of the crust | 2,200–2,400 kg/m$^3$ | 2,350 kg/m$^3$ |
| $\rho_2$ | Density at depth $d_t$ | 2,850–3,000 kg/m$^3$ | 2,900 kg/m$^3$ |
| $\rho_m$ | Magma density | 2,600–2,850kg/m$^3$ | 2610 kg/m$^3$ |
| *Buried dislocation* | | | |
| Strike | Strike (degrees east of north) for rift axis | 13.30–15.85° | 13.30° |
| $l_b$ | Dislocation locking depth | 8–13 km | 8.0 km |
| Opening | Net cumulative opening | 4–5 m | 5.0 m |
| Easting | Uncertainty in Easting location of axis at fixed latitude | ±2.5 km | 1.36 km |

(Sparks et al., 1980). To reflect uncertainty for magma *in situ*, we allow a slightly larger range of 2,600–2,850 kg/m$^3$, so that magma is negatively buoyant in the upper crust.

To summarize, we compute the stress before the diking event as a superposition of a tectonic stress field, derived from a tapered buried dislocation and a density structure that gives rise to a lithostatic pressure. The buried dislocation model is governed by the following parameters (see also Table 1): The depth to the top of the dislocation $l_b$, its strike and location (±2.5 km) with respect to Askja caldera center (Heimisson et al., 2015a). The lithostatic pressure depends on the two densities $\rho_1$ and $\rho_2$ and the transition depth $d_t$.

### 3.1.2. Inversion Procedure

The previous section described ranges of parameters that determine the remote stress field. Here we show how these ranges are narrowed to preferred estimates using InSAR and GPS data. We select 11 interferograms that have been processed and down sampled by Sigmundsson et al. (2015) and GPS displacements from 12 stations (Figure 1) that span the entire dike intrusion. The dike model is used to predict net GPS displacements and line of sight displacement for the 11 interferograms. We minimize an $L_2$ objective function

$$\chi^2 = (\boldsymbol{d} - \boldsymbol{G}_d(\boldsymbol{m}))^T \Sigma_{\boldsymbol{d}}^{-1} (\boldsymbol{d} - \boldsymbol{G}_d(\boldsymbol{m})), \tag{9}$$

where $\boldsymbol{G}_d$ represents the forward operator that maps a model parameter vector $\boldsymbol{m}$ to line of sight surface displacement and east, north, and up GPS components. The corresponding data are contained in vector $\boldsymbol{d}$. The variance-covariance matrix, $\Sigma_{\boldsymbol{d}}$, follows Sigmundsson et al. (2015) in estimating the spatial covariance of the InSAR data; the GPS error is assumed to be spatially uncorrelated.

To compute predicted displacements, three parameters are required in addition to those listed in Table 1: $\Delta V$, the volume change of a Mogi source representing caldera deflation at a fixed location (from Parks et al., 2017), $P(z_{LNB})$ from equation 1, and $L$ the dike length. The time span of the interferograms varies considerably with the later acquisition times ranging from 26 August to 20 September, 2014. The length of the dike likely did not change after 26 August (Sigmundsson et al., 2015; Spaans & Hooper, 2018), although, the dike pressure and the chamber volume were still evolving. $\Delta V$ is inherently time dependent because the acquisition times of the interferograms are variable. However, at this stage we treat $\Delta V$ as constant. Although this does not accurately capture the complicated near-field deformation, which was a combination of a caldera collapse and a deeper depressurization (Parks et al., 2017), it should approximately correct for the far-field displacement from the deeper depressurization.

$P(z_{LNB})$ changes with time and in the next section will be estimated as such. However, in this step of the inversion the goal is to estimate the time-independent parameters, and we thus take $P(z_{LNB})$ as constant between 26 August to 20 September. Although approximating $\Delta V$ and $P(z_{LNB})$ as time invariant results in additional misfit between model predictions and data, allowing for different values for every interferogram resulted in a model space that was too large to converge confidently. Most importantly, the values of $\Delta V$, $P(z_{LNB})$ estimated at this initial stage are not utilized in the subsequent time-dependent inversion.

The inversion procedure starts by finding a good fit to the data using a genetic algorithm (Goldberg & Holland, 1988); it then attempts to improve the fit further using a direct search algorithm

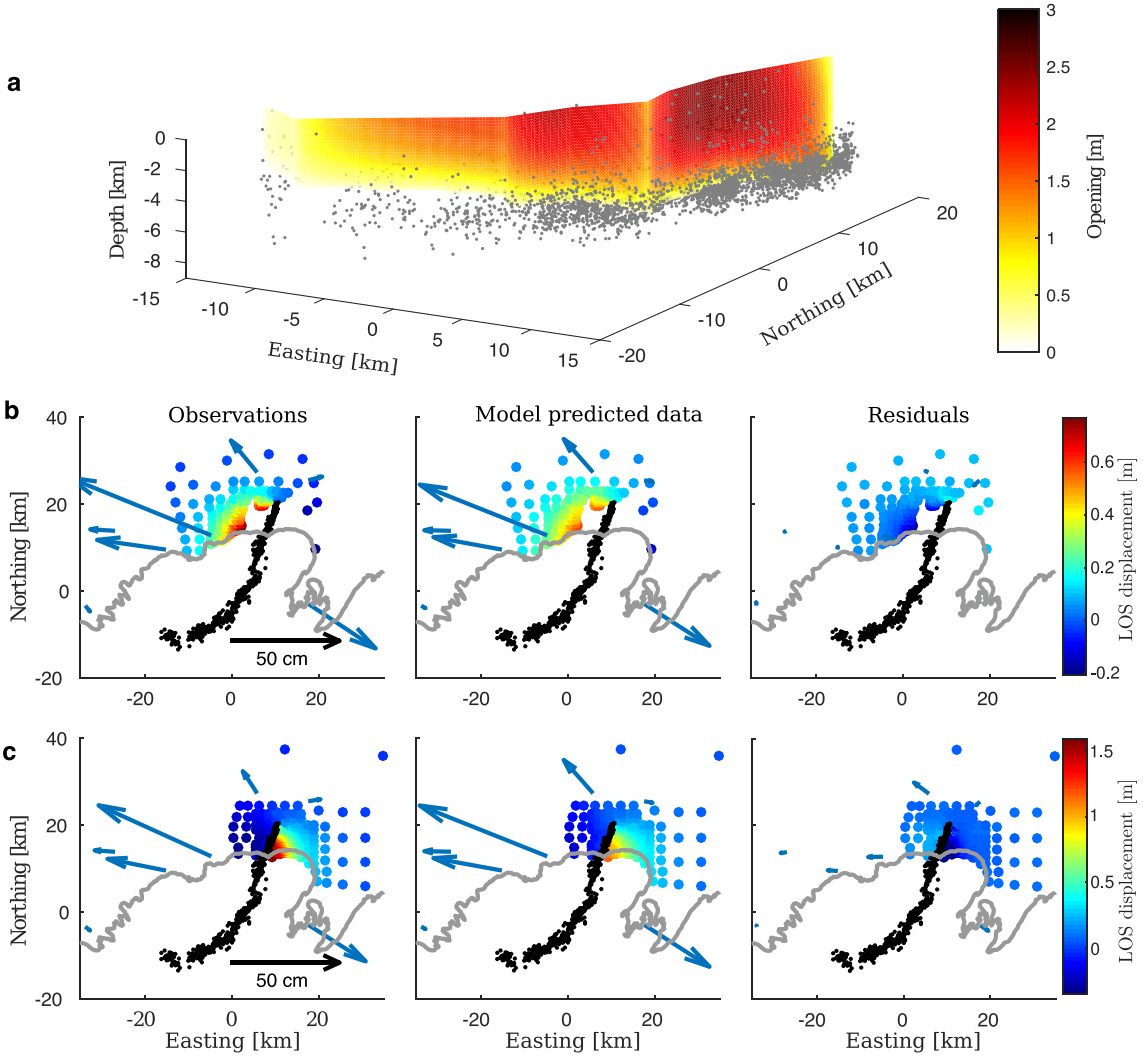


**Figure 6.** The static dike model (a) and comparison of the observations, model predicted data and residuals for TerraSAR-X (26 July 2012 to 4 September 2014, ascending) (b) and Cosmo-SkyMed (13–29 August 2014, descending) interferograms (c). Arrows indicate horizontal GPS displacements at the time of the final InSAR acquisition. The bottom edge of the model dike is roughly coincident with the seismicity.

(Audet & Dennis, 2002). Both steps enforce strict bounds on the parameter values (Table 1). Running this scheme repeatedly consistently converges to the same minimum, which we interpret as the global minimum. The optimal values for the stress model are reported in Table 1. These maximum likelihood values are used in the following, time-dependent inversion.

#### 3.1.3. Results: Stress Model

Figure 6 shows the opening distribution of the final dike model and two examples of interferograms used in the inversion. The lower tapered edge of the dike agrees well with the depth of earthquakes. This agreement is not enforced and the model space does allow for dikes that would extend substantially deeper or shallower. The deformation residuals indicate good agreement between observations and model predictions.

### 3.2. Time-Dependent Estimation of Dike Pressure and Stressing History

In this section, we estimate the dike pressure $P(z_{LNB}, t)$ from continuous GPS data. As discussed previously, this pressure is assumed constant along the dike length. From the time evolution of dike pressure we produce a temporal model of dike opening in space and time. This model is then used to compute the stressing history in each voxel as functions of time during the intrusion.

The 8 hr GPS time series is interpolated into 100 time steps, corresponding roughly to 1 point per 4 hr. This upsampling was necessary to resolve characteristics of the seismicity that occur on time scales shorter than

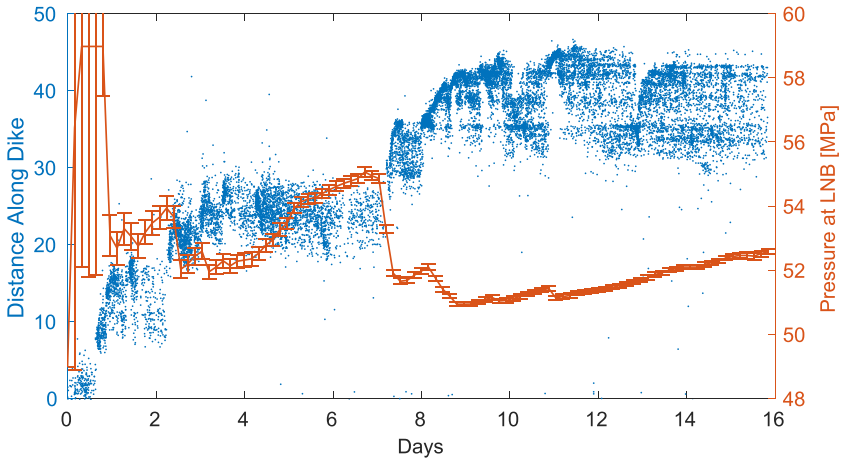


**Figure 7.** Comparison of the inferred time-dependent magma pressure at the LNB, based on inversion of time-dependent GPS data and the space-time evolution of the seismic swarm. Error bars are one standard deviation. As the dike advances the pressure drops and when arrested the pressure builds up. The dike model is magmastatic and the pressure is assumed constant along the dike length at any given time

8 hr in section 3.3. For each time step the length of the dike $L(t)$ is determined by the advancing seismic swarm; the magma is assumed to be 1 km behind the location of the highest seismicity rate during that time step. $L(t)$ does not change if the point of highest seismicity rate retreated relative to the previous position. Thus, the dike can only lengthen or stay constant.

At each time step the magma pressure at the LNB $P(z_{LNB}, t)$ is optimized by fitting the GPS data. An objective function of the same form as equation (9) is minimized. At the beginning of each time step, we find the least squares solution for the volume change of a Mogi source, representing the deflating magma reservoir. Two stations VONC and HAUC (Figure 1) are used to constrain this volume change since they are close to the caldera and show limited sensitivity to the dike. The predicted displacements from the Mogi source are then used to correct the GPS time series at other stations before the time-dependent dike inversion is performed. We apply this correction instead of inverting for $P(z_{LNB}, t)$ and volume change of the Mogi source simultaneously due to the computational requirements needed to converge in this time-varying 2-D model space. Furthermore, the deflation signal away from the caldera is much less than the dike signal. Note that because the dike geometry (i.e., which dislocations open) depends on the pressure $P(z_{LNB}, t)$, this step is a nonlinear inversion.

In summary, from the inversion of time-dependent GPS data we obtain $P(z_{LNB}, t)$, while $L(t)$ is determined from the location of the maximum seismicity rate. This, along with the time-independent parameters (determined in section 3.1.3) is sufficient to derive an opening distribution for the dike at each time step. Using elastic Green's functions the dike opening is used to compute the full stress tensor at Gauss points in each voxel surrounding the dike. The time history of the stress tensor at each Gauss point is used in the next step to compute the cumulative number of seismic events and compare to observations (section 3.3).

We found that it was not sufficient to represent the stressing history in only 100 time steps. We thus assume that between time steps the dike grows at a constant velocity and evaluate the stress, at each Gauss point, every 200 m of dike advance. The procedure results in a stressing history of ~1,000 time steps. We found that the results are insensitive to downsampling the stressing history by 50%, which implies convergence of equation (6). Several tests were made to check errors associated with the calculation of $N$ (equation (7)); this included changing the size of the dike elements, and varying the number of Gauss points and voxel size. We found that the current scheme: dislocations with an edge length of 200 m, voxels with a characteristic length of 1,500 m and 3 point Gaussian quadrature (27 points in each voxel), resulted in a numerical error much smaller than the data variance.

#### 3.2.1. Results

Results for $P(z_{LNB}, t)$ are shown in Figure 7, with an estimate of uncertainty derived by fixing the dike geometry to the optimal value found by the nonlinear inversion scheme in Section 3.2. With fixed dike geometry,

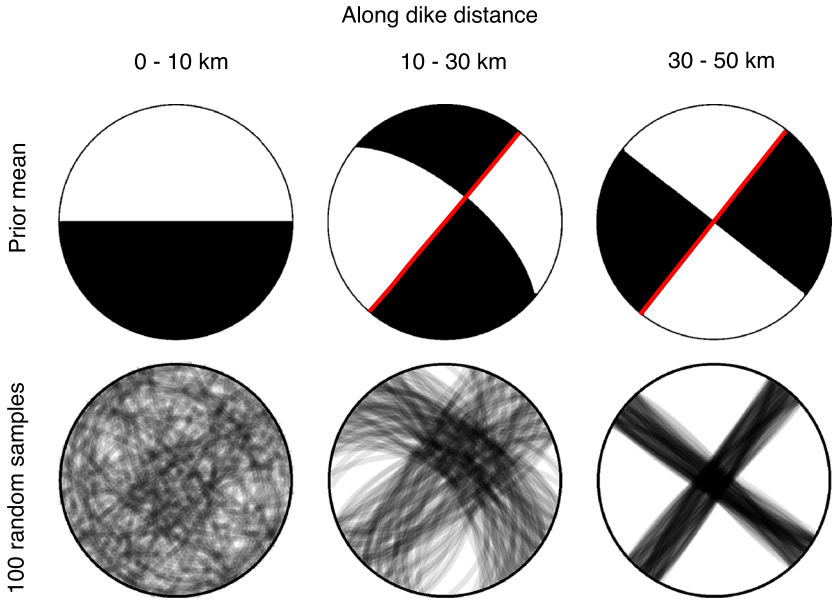


**Figure 8.** Visualization of the prior distributions on focal mechanisms. Top row shows the focal mechanism corresponding to the mean of the strike, dip, and rake priors. Red line indicates the assumed fault plane. Bottom row shows 100 random samples from the prior distributions. Columns correspond to distance along dike length: the mechanism is uncertain for range 0–10 km, reasonably well constrained for 10–30 km, and tightly constrained for >30 km (Ágústsdóttir et al., 2019).

the inverse problem is linear, and propagation of uncertainties in the GPS data to errors in the pressure estimate is straightforward. This reveals that initially, when the dike is short, the pressure is highly uncertain.

Figure 7 shows that the dike pressure increased during pauses in dike advance and dropped once rapid propagation recommenced, consistent with the interpretation of Sigmundsson et al. (2015). During the pauses in propagation, inflow of additional magma continued resulting in increased pressure, but when the dike advanced, the pressure decreased. These processes are not explicitly prescribed by the dike model but are required to fit the GPS data. Comparison to Figure 4 reveals that at times when the pressure decreased, the GPS displacements generally increased. This is simply because far-field displacements are mostly sensitive to the dike volume and the crack surface area increased during the pressure drops, more than compensating for the pressure reduction. All GPS stations that recorded the entire event are in the far field, near-field stations like URHC (Figure 1) were transformed from campaign benchmarks to continuous stations only once the dike was fully formed. It is worth reiterating that the results in Figure 7 are only constrained by inverting the continuous GPS, not the seismicity data. The seismicity at this stage is used only to determine the location of the dike tip.

### 3.3. Seismicity Model: Inversion in Voxels for Seismic Source and Frictional Properties

In the previous two steps, we constrained the background stress field and the time-dependent dike-induced stresses based on geodetic and seismic data. In this section, we use those estimates to predict the cumulative number of earthquakes in each voxel ($N$ in equation (3)). Although many fields and parameters have been constrained in the previous steps, there are six additional parameters that relate to $N$, three characterizing the receiver fault orientation: strike, dip, and rake, and three related to frictional properties and background stressing rate: $A$, $\alpha$, and $r$. We use a Markov Chain Monte Carlo (MCMC) approach to estimate posterior probability density functions for fault orientation (strike, dip, and rake) from focal mechanisms and earthquake production parameters ($A$, $r$, and $\alpha$). All prior distributions are taken to be uniform with hard bounds, which are described below.

We estimate strike, dip, and rake based on focal mechanisms and inferred fault planes from Ágústsdóttir et al. (2019). For the first 10 km of the dike, a voxel can have essentially any fault orientation that could be considered reasonable for a rift setting (Figure 8); this is done to reflect the highly variable and uncertain focal mechanisms in this area. We allow either strike slip (both left and right lateral), normal or oblique (between strike slip and normal) with the dip constrained to be between 60° and 90°. For the distance range

of 10–30 km the focal mechanisms exhibit right lateral strike slip with a strike of ~40°. However, we allow for uncertainty in dip, strike, and rake (Figure 8) to reflect the focal mechanism variability. For the final 30 km, the focal mechanisms are tightly constrained, which translates into low variance in the prior distributions (Figure 8).

The prior for the constitutive frictional parameter $A$ is set to a wide range $10^{-5}$ to 0.02. The upper limit represents the highest values from lab experiments under elevated pore fluid pressure and temperature (Blanpied et al., 1991). The lower limit is estimated from the values of $A\sigma_0$ that are commonly inferred when the Dieterich (1994) theory is applied to field data (Hainzl et al., 2010). The parameter $\alpha$ is related to instantaneous changes in the frictional state due to changes in normal stress (Linker & Dieterich, 1992). We set $\alpha$ to a range of 0–0.5. We reject seismicity models where $\tau_0$, $\mu$, $\dot{\tau}_b$ or $\dot{s}_b$ are negative, which enforces additional constraints locally on possible fault planes that are not reflected in Figure 8, and guarantee that only fault orientations are considered that are subject to stresses favorable for slip.

The prior on background seismicity rate ranges from $2 \cdot 10^{-2}$ to $10^{-5}$ events per year for a voxel of average size. The seismicity model includes ~500 voxels, which means that at the upper bound we would expect on the order of 10 events per year. Prior to the 2014 diking event, no seismicity had been detected on large parts of the eventual dike path (Ágústsdóttir et al., 2019). We estimate the magnitude of completeness for the dike-induced events to be $M_c = 1$, considerably lower than that for the national seismic network. Small background events may, therefore, not have been detected. Nevertheless, it is likely that 10 events per year would have resulted in some large enough to be detected over the 23 years of seismic monitoring prior to the 2014 Bárðarbunga intrusion. However, the population of seismic sources (see Heimisson, 2019, for precise definition) may not have been sufficiently stressed prior to the intrusion to produce earthquakes at a constant rate. Indeed, Figure 5 suggests that in most places the background shear to normal stress ratio was fairly small. In this case, a steady-state background rate would not have been reached prior to the diking event (Heimisson & Segall, 2018) (see section 4.1 for further discussion) and could be much higher than what can be inferred from observations. In this context, the background rate is the steady-state seismicity rate that would eventually occur if the populations of seismic sources were subject to constant background stressing rate. We thus conclude that a broad a priori range is needed to reflect this uncertainty.

Sampling of the PDFs is done using an ensemble sampler algorithm proposed by Goodman and Weare (2010) (using the implementation of; Foreman-Mackey et al., 2013). The algorithm samples the log posterior distribution for the $n$th voxel:

$$\log(p(\boldsymbol{m}^n, \boldsymbol{\sigma}^n | \boldsymbol{d}^n)) = -\frac{1}{2} \sum_i \left( \frac{N_i^n - \tilde{\mathrm{N}}^n(\boldsymbol{m}^n, t_i)}{\sigma_i^n} \right)^2 - \sum_i \log\left(\sqrt{2\pi}\sigma_i^n\right) + \log(p(\boldsymbol{m}^n)), \tag{10}$$

where $N_i^n$ is the cumulative number of seismic events at the $i$th time step and $\sigma_i^n$ is the corresponding standard deviation. $\tilde{\mathrm{N}}(\boldsymbol{m}^n, t_i)$ represents the forward operator that takes in the six aforementioned model parameters, $\boldsymbol{m}^n$ (as well as the precomputed space-time variable stress field) and predicts the cumulative number of events in each voxel from equation (7). Finally, $p(\boldsymbol{m}^n)$ is the prior probability distribution of the model parameters in the $n$th voxel.

#### 3.3.1. Results: Voxel Inversion

Inversion results (Figure 9) exhibit high spatial variability in many parameters of interest. The maximum a posteriori estimate of $A$ ranges from typical laboratory values ($A \sim 0.01$) to much smaller values ($A \sim 10^{-5}$). The parameter estimates are spatially correlated, although no such correlation or smoothing is prescribed in the inversion. This may suggest robustness in the inversion, although, if some models assumptions are incorrect, this could systematically bias parameter estimates. One such bias may stem from the assumed dike tip underpressure, which was taken to be the end member case of negligible tip pressure ($\Delta P = -\sigma$). With higher dike tip pressure ($\Delta P = P_f - \sigma$), the near-field stress perturbations are lower and distributed differently, which may systematically bias $A$. However, most of the recorded earthquakes are not located at the dike tip, but at the bottom of the dike where the opening tapers due to the vertical gradient in overpressure (Figure 6a). Thus, the influence of the leading dike tip on the temporal evolution of the earthquakes may be modest.

In the supporting information, we show the median value for each distribution, as well as 5% and 95% percentile values (Figures S1–S3). Figure 9 demonstrates that in the vast majority of voxels, the seismicity

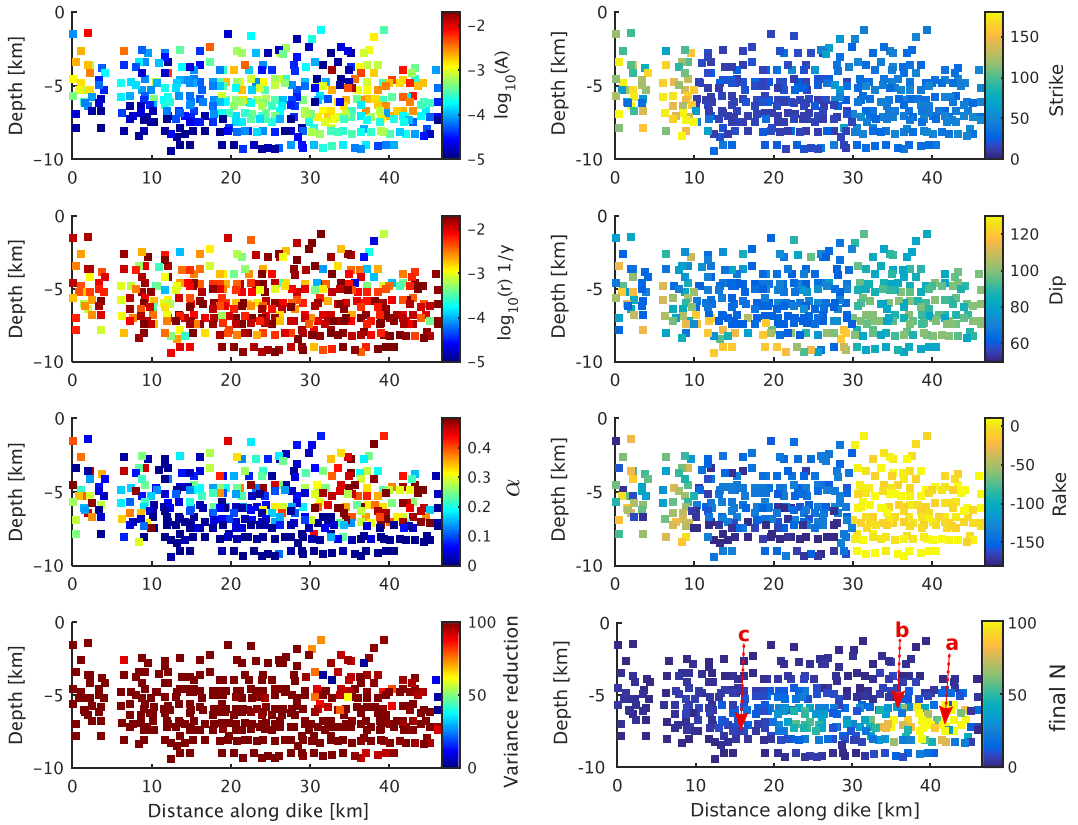


**Figure 9.** Maximum a posteriori (MAP) values for model parameters estimated in each voxel, along with variance reduction and final cumulative number of events in the bottom row. Labels *a*, *b*, and *c* and corresponding arrows (bottom right) indicate the locations of voxels shown in Figure 10. Each square represents the center of a voxel projected in depth versus distance-along-dike coordinates.

model can explain most of the variance in the data. Figure 10 shows the probability distributions for three different voxels, which vary substantially in temporal behavior and the final cumulative number of events. This figure highlights the influence of the cumulative number of events on the width of the posterior distributions. There tends to be a narrow range of model parameters that can fit voxels with more than 100 events, whereas voxels with only a handful of events have much broader distributions (see also supporting information Figures S2 and S3).

The fit to the cumulative number of events curves, $N(t)$, is generally good (Figures 9 and 10). To further investigate if the seismicity model resolves important space-time characteristics of the seismicity induced by the Bárðarbunga dike, we generate a synthetic catalog. To do so, we round each predicted $N(t)$ time series from the maximum a posteriori model to the nearest integer, rendering time-discrete events. We the assign a time to each event by sampling from a uniform distribution with bounds at the previous and subsequent time steps. This procedure reveals that many of the important characteristics of the observed seismicity are reproduced by the model (Figure 11). Most importantly, the seismicity model predicts that actively intruding segments remain seismically active while all previous segments become more or less aseismic. The model generally matches the total number of events in each voxel quite well, as reflected in the variance reduction (Figure 9). For computational reasons, we only run the inversion on roughly half the voxels and, therefore, do not match the absolute number of events in the catalog. However, the voxels selected for MCMC sampling are picked to represent all seismically active regions surrounding the dike in an unbiased manner. For a 3-D view of the dike model and simulated seismicity see supporting information Movie S1.

## 4. Discussion

### 4.1. Background Seismicity Rate

One of the most significant uncertainties in this study is the background seismicity rate in each voxel. Very few events had been previously detected in the area where the dike propagated. Does that mean the

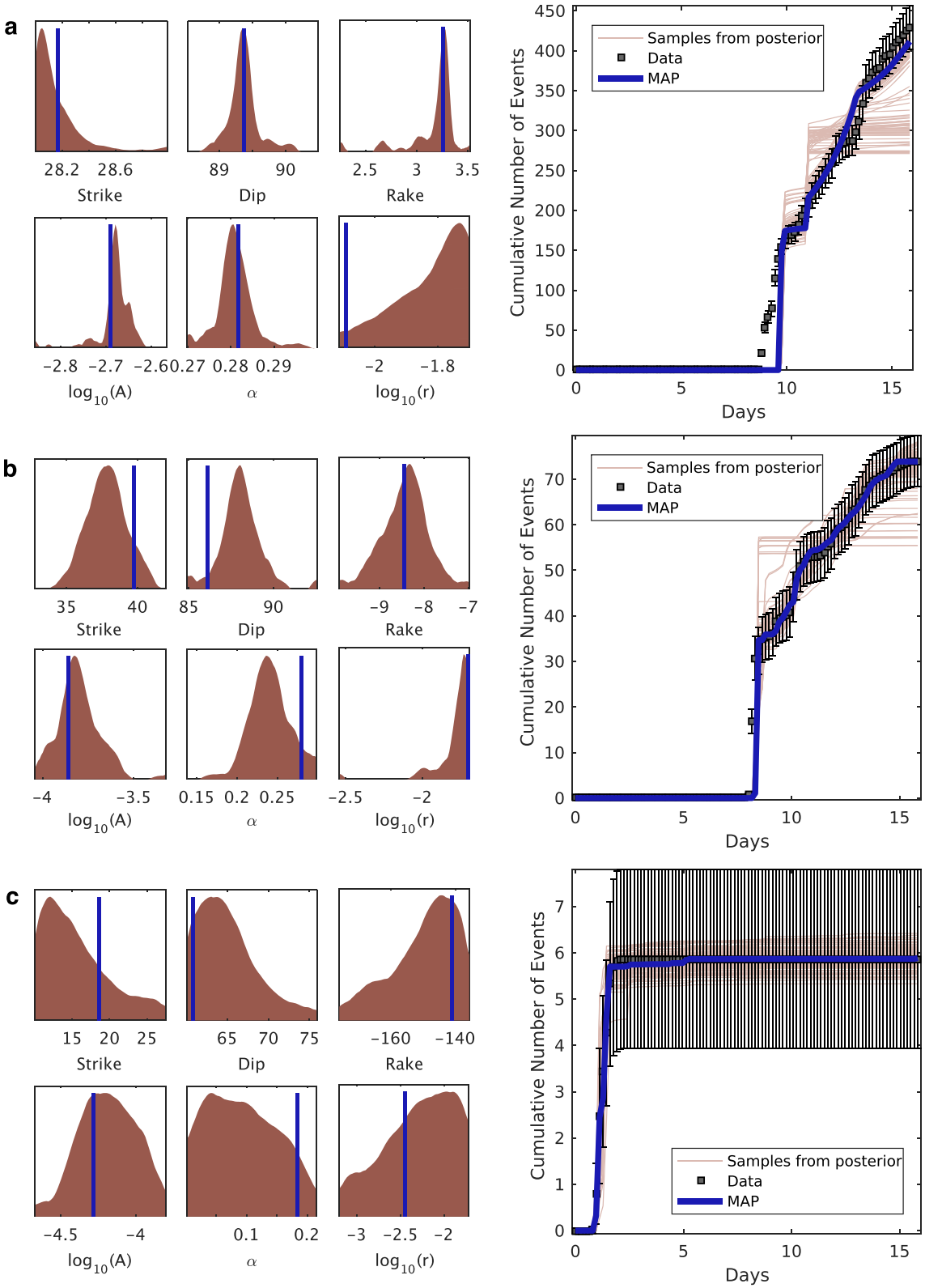


**Figure 10.** Parameter distributions (left column) and predicted/observed cumulative number of events for three voxels (a–c; locations shown in Figure 9, bottom right), vertical bar marks the MAP value and distributions are shown over their 95% confidence intervals. Voxels were picked to illustrate a wide range of cumulative number of events with panel **a** showing the voxel with the maximum number of events. The range of acceptable models strongly depends on the cumulative number of events.

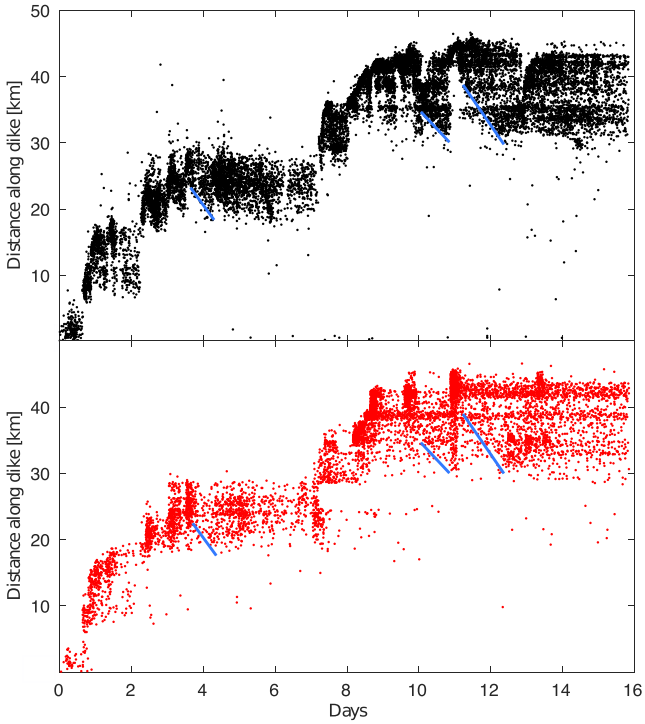


**Figure 11.** Comparison of observed and predicted seismicity interpreted in the form of individual events. Black dots show detected earthquakes; red dots are simulated events based on the MAP model prediction of the cumulative number of events. Blue lines indicates examples of backpropagation of seismicity and the corresponding locations in the predicted seismicity (see section 4.2 for discussion of the backpropagation).

background seismicity rate is zero? One possible explanation is that it is very low, with no events large enough to be detected by the national network. The temporary seismic network in the area during the intrusion was able to detect much smaller events than the Icelandic permanent seismic network (SIL network). However, the MCMC sampling suggests that most voxels have a background seismicity rate near the upper limit, set at one event per 50 years. If that is correct, it is unlikely that no events would have been detected before 2014. We thus favor the explanation that seismic sources were not sufficiently stressed to produce earthquakes prior to the intrusion, but once exposed to the large dike-induced stresses were driven to failure. We made some attempts at estimating this threshold using a nonconstant background rate model (equation (34) in Heimisson & Segall, 2018). However, due to uncertainty in the dike tip location and the fact that the two predictions are equivalent once the threshold is reached, these attempts did not give meaningful results and generally predicted a negligible threshold. In contrast, if we had placed the dike tip slightly ahead of the swarm, then such a threshold would be required. We conclude that the dike and post rifting period release most ofthe interdiking stresses leaving the crust in a low-stress state. Indeed, previous studies found the dike opening agreed well with the expected strain accumulation since the last intrusion (Ruch et al., 2016). The absence of background seismicity prior to the diking event does not negate the use of the modified Dieterich theory, provided that the stress changes due to the dike are sufficient to elevate the population well above steady-statefriction (Heimisson & Segall, 2018).

### 4.2. Segmentation of Seismicity and Backpropagation

The seismicity model reproduces the segmentation of the seismicity along the dike, where the newest segment remains seismically active until the next segment is formed. Once the formation of a new segment is underway very few earthquakes occur in the previous segments (Figure 11). This behavior can be physically understood from Figure 7, where in general the pressure drops as the dike grows, although it increases transiently when the dike stalls. During a pause, the seismic sources are exposed to increasing stresses as the pressure recovers. The seismicity rate $R$ depends on the integral of the stress kernel $K(t)$ (equation (4)):

$$\frac{R}{r} = \frac{K(t)}{1 + \frac{\dot{s}_b}{A\sigma_0}\int_0^t K(t')dt'}, \tag{11}$$

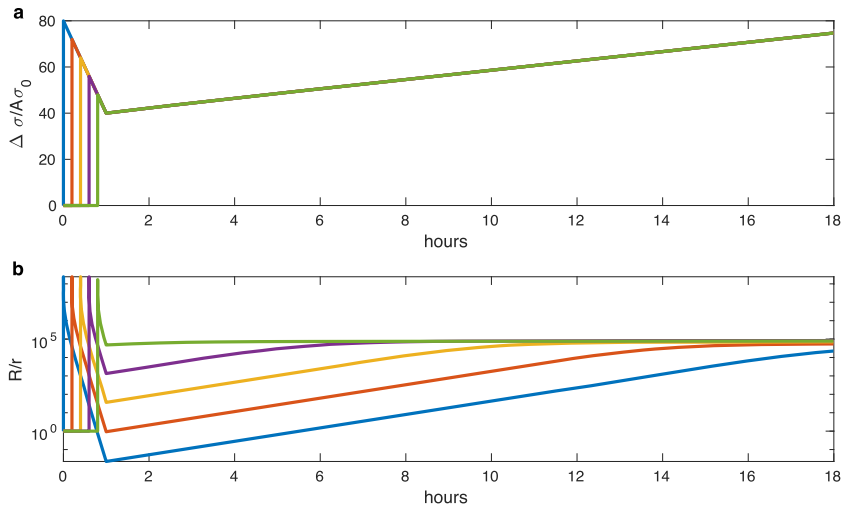


**Figure 12.** Idealized stressing histories that produce backpropagation of seismicity at roughly constant speed. (a) Stress history at different points adjacent to the dike; (b) corresponding seismicity rate. As the dike advances the pressure decreases and the peak stress sensed by seismic sources decreases with propagation distance (blue to green lines). Once the dike propagation halts, a slow repressurization begins, which is approximately the same for all source populations. Each population of sources is only significantly reactivated once the stress reaches the previous peak value.

which means that during the pauses the integral in the denominator increases and, in physical terms, the population develops a stress memory or threshold, and will not be significantly activated again unless the stress change exceeds the previous peak. In summary, as a segment of the dike intrudes, the pressure increases and reaches a maximum before the next segment is formed. Because the pressure never sufficiently exceeds the previous maximum, the previous segments are not reactivated seismically. Such a stress memory (Kaiser effect) has been previously identified in triggering of volcano-tectonic earthquakes (Heimisson et al., 2015b).

In some parts of the dike, where abrupt changes in direction (or kinks) occur, there is also a significant stress rotation that affects source populations near the kink. For example, a very clear shutoff of seismicity occurs in the simulated catalog (Figure 11) around Day 7.5 and distance 25–29 km. This abrupt shutoff is due to the geometry of the kink, which causes a stress shadow. However, in most other parts of the dike, the segmentation in seismicity is caused by the stress memory effect. Magma solidification in the narrower lower and/or upper reaches of the dike may also play a role, by changing the compliance of the dike, and by altering the location of the largest induced stresses. However, solidification is not included in our model and is thus not needed to explain the large scale segmentation of the seismicity.

Another striking feature of the seismicity is several occurrences of backward propagation at an approximately constant speed. Three of these are marked in Figure 11. The simulated catalog shows some evidence for backpropagations at these times; however, this is not as clear as it is in the observed seismicity. The difference between model and observations may be in part due to discretization in space and time, which limit the resolution of the simulated catalog. Alternatively, the backpropagation could be due to physics which are not modeled in this study.

We suggest that backpropagation may also be explained by stress memory effects, as follows. When the dike advances the pressure drops, from Figure 7, we estimate that the pressure drop is about ~2 MPa/hr. The stress sensed by the populations of seismic sources drops approximately proportionally. Once the dike halts it begins repressurizing (at a rate of about ~0.1 MPa/hr). Thus, seismic sources along the length of the dike that have experienced different peak stresses, with more distal sites experiencing lower peak stress, will reactivate at different times. To test this hypothesis, we compute the seismicity rate for hypothetical populations that have been exposed to varying peak stress that decreases with dike propagation distance. Once a minimum stress is reached, all populations are subject to the same slow repressurization (Figure 12). Due to the stress memory effect, the populations are reactivated at different times and together produce backpropagation of seismicity at a constant speed that is proportional to the repressurization rate. Further

study of the backpropagation is needed, in particular, to exclude other potential explanations and to explore more direct comparison with data at finer spatial resolution.

It is generally agreed that the propagation of dike-induced seismic swarms result directly from the propagation of the dike. We further suggest that many spatiotemporal complexities in the dike-induced seismicity result largely from the interplay of time-dependent pressure and stress memory effects. As a consequence the turning on and off of seismicity may indicate transient pressure changes, where seismicity rate increase rapidly upon exceeding previous pressure levels. In summary, the seismicity does not directly measure the current state of stress at a point in the crust but rather responds to the recent stressing history of that point. Additional information from geodetic measurements is, therefore, essential to deconvolve the stressing history and the observable seismicity.

### 4.3. Secondary Triggering

Where the Dieterich (1994) theory has been used in a similar manner as in this study, it has been noted that there may be biases due to source interactions and secondary events (Inbal et al., 2017; Segall et al., 2013), effects that are not included in the theory. Several algorithms have been developed to decluster earthquakes and remove aftershocks or secondary events, but each method is based on different assumptions and generally produce different results when applied to the same catalog (Marsan & Lengline, 2008). Moreover, most declustering methods are made to separate mainshocks from aftershocks. Dike intrusions are striking examples of extremely strong spatial and temporal clustering not primarily driven by mainshock-aftershock triggering, but by the time evolution of the stress field induced by the dike. Thus, it can be argued that most declustering methods are not appropriate for such a sequence.

Furthermore, Heimisson (2019) challenged the view that declustering is required when applying the Dieterich theory. He showed, under a few assumptions that hold fairly generally, that populations of seismic sources with and without interactions produce the same seismicity rate when perturbed, if they have the same background seismicity rate. This indicates that a population with interactions can be approximated as a population without interactions with the same long-term average background seismicity rate. In addition, Heimisson (2019) showed that interaction between populations in a spatially heterogeneous stress field do not change the absolute number of events on a regional scale for times $t \gg t_a$. This suggests that interactions do not change the absolute number of events, although they may somewhat change their temporal and spatial distribution. These results indicate that the assumption of non-interacting sources may not be as consequential as it seems. Given this, we suggest that using the full seismic catalog introduces less bias than declustering, which may likely remove physically relevant spatial and temporal correlations in the seismicity.

### 4.4. Validation of Dieterich (1994)

Our results support the applicability of the Dieterich (1994) theory to temporally complicated and large magnitude stress changes. The results show that the theory is consistent with the cumulative number of events in most voxels even after independent observations such as GPS and InSAR have been used to constrain the complete stressing history in each voxel. In that sense, the results provide significant observational validation of the theory since the temporal evolution of the cumulative number of events is strongly controlled by stressing history. However, in order to match the observations, it is necessary to constrain time-independent parameters in each voxel, and some of those parameters must be spatially heterogeneous (Figure 9).

### 4.5. Further Development of Joint Inversions for Dike Propagation

Segall et al. (2013) proposed imaging a propagating dike through simultaneous joint inversion of both earthquakes and deformation, where deformation is sensitive to the inflation of the dike, but earthquakes better constrain the location of the dike tip. They tested the method on the Father's Day dike intrusion on Kilauea, which had about 200 recorded earthquakes, and simultaneously fit the cumulative number of events and GPS time series assuming spatially uniform background stresses and frictional parameters. Our study demonstrates, however, that voxels with few events can be fit with a wide range of parameters, but when the number of events exceeds about 100, the fit can be achieved only within a very narrow range of parameters. Performing such joint inversion for the 2014 Bárðarbunga dike would require accounting for spatially variable frictional properties, initial stress, or short wavelength features in the dike-induced stress in some stochastic manner, since uniform frictional properties are not consistent with the observations.

Additional improvements in the joint inversion strategy might involve estimating the receiver fault orientation directly based on the observed seismicity and a model of the dike-induced stress changes. We made some attempts to constrain the activated fault planes based on the dike model and time history of seismicity in each voxel. Preliminary results suggested that sometimes the correct fault plane was recovered, however frequently the inversion converged to other fault planes that fit the data equally well, or better. While the preliminary results were promising, we concluded that this was beyond the scope of the study and instead constrained the fault planes to be consistent with the observed focal mechanisms.

Looking ahead, one goal of joint inversions of seismic and geodetic data to image a dike would be to do so in real time. This task involves further challenges, in particular, related to the lack of prior knowledge of the dike path. In some places, dikes propagate along a rift zone, such that the path may be known reasonably beforehand, but because voxels should not intersect the dike plane that knowledge of the trajectory would need to be precise. In the more general case, the problem will require adaptive meshing that can follow the dike as it propagates.

## 5. Conclusions

We have developed methodology for analyzing deformation and seismicity together with a single physics-based dike model. The approach makes use of geodetic data (InSAR and GPS) and seismic data (earthquake locations and focal mechanisms) to construct a dike model that predicts both deformation and seismicity. The model was applied to the spatially and temporally complex 2014 Bárðarbunga diking event. The results shed light on the physics of dike-induced earthquakes, which are found to be consistent with elastic stress transfer onto preexisting faults, as previously suggested (e.g., Rubin & Gillard, 1998).

We applied the modified Dieterich theory (Heimisson & Segall, 2018) to a more complicated stressing history than previous studies. The inversion of the cumulative number of earthquakes provides a rare insight into the frictional properties of the crust. We find that the constitutive parameters $A$ and $\alpha$ exhibit considerable variability, but are spatially correlated. The correlation is not imposed through spatial smoothing and may suggest robustness of the inversion process and methodology.

The GPS inversion indicates that on average magma pressure drops when the dike propagates and recovers when the dike stalls. This may explain the characteristic segmentation of the Bárðarbunga dike as a manifestation of a stress threshold or memory effect, because the stress never becomes sufficiently large to reactivate the previous segments.

**Acknowledgments**
We thank Tim Greenfield, Bob White, and Thorbjörg Águstsdóttir for providing access to earthquake locations and magnitude estimates prior to publication. We also thank Sigrún Hreinsdóttir for providing the 8 hr GPS time series and Andy Hooper for the processed and downsampled interferograms. We thank Jean-Luc Got and an anonymous reviewer for their constructive remarks. All data used in this study can be found under following references (Ágústsdóttir et al., 2019; Greenfield et al., 2018; Sigmundsson et al., 2015). This research was supported by NASA under the NASA Earth and Space Science Fellowship Program (Grant NNX16AO40H) and NASA ROSES ESI (Grant NNX16AN08G).

## References

Ágústsdóttir, T., Woods, J., Greenfield, T., Green, R. G., White, R. S., Winder, T., et al. (2016). Strike-slip faulting during the 2014 Bárðarbunga-Holuhraun dike intrusion, central Iceland. *Geophysical Research Letters*, *43*, 1495–1503. https://doi.org/10.1002/2015GL067423

Ágústsdóttir, T., Woods, J., Winder, T., White, R. S., Greenfield, T., & Brandsdóttir, B. (2019). Intense seismicity during the 2014–15 Bárðarbunga–Holuhraun Rifting Event, Iceland, reveals the nature of dike-induced earthquakes and caldera collapse mechanisms. *Journal of Geophysical Research: Solid Earth*, *124*, 8331–8357. https://doi.org/10.1029/2018JB016010

Árnadóttir, Þ., Jiang, W., Feigl, K. L., Geirsson, H., & Sturkell, E. (2006). Kinematic models of plate boundary deformation in southwest Iceland derived from GPS observations. *Journal of Geophysical Research*, *111*, B07402. https://doi.org/10.1029/2005JB003907

Audet, C., & Dennis, Jr J. E. (2002). Analysis of generalized pattern searches. *SIAM Journal on Optimization*, *13*(3), 889–903. https://doi.org/10.1137/S1052623400378742

Blanpied, M., Lockner, D., & Byerlee, J. (1991). Fault stability inferred from granite sliding experiments at hydrothermal conditions. *Geophysical Research Letters*, *18*(4), 609–612. https://doi.org/10.1029/91GL00469

Brandsdottir, B., & Einarsson, P. (1979). Seismic activity associated with the September 1977 deflation of the Krafla central volcano in Northeastern Iceland. *Journal of Volcanology and Geothermal Research*, *6*(3–4), 197–212. https://doi.org/10.1016/0377-0273(79)90001-5

Carlson, R. L., & Herrick, C. N. (1990). Densities and porosities in the oceanic crust and their variations with depth and age. *Journal of Geophysical Research: Solid Earth*, *95*(B6), 9153–9170. https://doi.org/10.1029/JB095iB06p09153

Cayol, V., & Cornet, F. H. (1998). Three-dimensional modeling of the 1983–1984 eruption at Piton de la Fournaise Volcano, Réunion Island. *Journal of Geophysical Research*, *103*(B8), 18,025–18,037. https://doi.org/10.1029/98JB00201

Christensen, N. I., & Wilkens, R. H. (1982). Seismic properties, density, and composition of the Icelandic crust near Reydarfjörður. *Journal of Geophysical Research*, *87*(B8), 6389–6395. https://doi.org/10.1029/JB087iB08p06389

Dieterich, J. (1994). A constitutive law for rate of earthquake production and its application to earthquake clustering. *Journal of Geophysical Research*, *99*(B2), 2601–2618. https://doi.org/10.1029/93JB02581

Drouin, V., Sigmundsson, F., Ófeigsson, B. G., Hreinsdóttir, S., Sturkell, E., & Einarsson, P. (2017). Deformation in the Northern Volcanic Zone of Iceland 2008–2014: An interplay of tectonic, magmatic, and glacial isostatic deformation. *Journal of Geophysical Research: Solid Earth*, *122*, 3158–3178. https://doi.org/10.1002/2016JB013206

Du, Y., & Aydin, A. (1992). Three-dimensional characteristics of dike intrusion along the northern Iceland Rift from inversion of geodetic data. *Tectonophysics*, *204*(1), 111–121. https://doi.org/10.1016/0040-1951(92)90273-9

Fialko, Y. A., & Rubin, A. M. (1999). What controls the along-strike slopes of volcanic rift zones? *Journal of Geophysical Research*, *104*(B9), 20,007–20,020. https://doi.org/10.1029/1999JB900143

Foreman-Mackey, D., Hogg, D. W., Lang, D., & Goodman, J. (2013). Emcee: The MCMC hammer. *Publications of the Astronomical Society of the Pacific*, *925*(125), 306.

Goldberg, D. E., & Holland, J. H. (1988). Genetic algorithms and machine learning. *Machine learning*, *3*(2), 95–99.

Goodman, J., & Weare, J. (2010). Ensemble samplers with affine invariance. *Communications in applied mathematics and computational science*, *5*(1), 65–80.

Got, J.-L., Carrier, A., Marsan, D., Jouanne, F., Vogfjörd, K., & Villemin, T. (2017). An analysis of the nonlinear magma-edifice coupling at Grímsvötn volcano (Iceland). *Journal of Geophysical Research: Solid Earth*, *122*, 826–843. https://doi.org/10.1002/2016JB012905

Green, R. G., Greenfield, T., & White, R. S. (2015). Triggered earthquakes suppressed by an evolving stress shadow from a propagating dyke. *Nature Geoscience*, *8*(8), 629–632. https://doi.org/10.1038/ngeo2491

Greenfield, T., White, R. S., Winder, T., & Ágústsdóttir, T. (2018). Seismicity of the Askja and Bárðarbunga volcanic systems of Iceland, 2009–2015. *Journal of Volcanology and Geothermal Research*. 0377-0273, 106432. https://doi.org/10.1016/j.jvolgeores.2018.08.010

Guðmundsson, M. T., & Högnadóttir, Þ. (2007). Volcanic systems and calderas in the Vatnajökull region, Central Iceland: Constraints on crustal structure from gravity data. *Journal of Geodynamics*, *43*(1), 153–169. https://doi.org/10.1016/j.jog.2006.09.015 hotspot Iceland.

Hainzl, S., Steacy, S., & Marsan, D. (2010). Seismicity models based on Coulomb stress calculations. Community Online Resource forStatistical Seismicity Analysis, https://doi.org/10.5078/corssa-32035809. [Available at http://www.corssa.org.]

Hartley, M. E., & Thordarson, T. (2013). The 1874–1876 volcano-tectonic episode at Askja, North Iceland: Lateral flow revisited. *Geochemistry, Geophysics, Geosystems*, *14*, 2286–2309. https://doi.org/10.1002/ggge.20151

Heimisson, E. R. (2019). Constitutive law for earthquake production based on rate-and-state friction: Theory and application of interacting sources. *Journal of Geophysical Research: Solid Earth*, *124*, 1802–1821. https://doi.org/10.1029/2018JB016823

Heimisson, E. R., Einarsson, P., Sigmundsson, F., & Brandsdóttir, B. (2015b). Kilometer-scale Kaiser effect identified in Krafla volcano, Iceland. *Geophysical Research Letters*, *42*, 7958–7965. https://doi.org/10.1002/2015GL065680

Heimisson, E. R., Hooper, A., & Sigmundsson, F. (2015a). Forecasting the path of a laterally propagating dike. *Journal of Geophysical Research: Solid Earth*, *120*, 8774–8792. https://doi.org/10.1002/2015JB012402

Heimisson, E. R., & Segall, P. (2018). Constitutive law for earthquake production based on rate-and-state friction: Dieterich 1994 revisited. *Journal of Geophysical Research: Solid Earth*, *123*, 4141–4156. https://doi.org/10.1029/2018JB015656

Hooper, A., Ófeigsson, B., Sigmundsson, F., Lund, B., Einarsson, P., Geirsson, H., & Sturkell, E. (2011). Increased capture of magma in the crust promoted by ice-cap retreat in Iceland. *Nature Geoscience*, *4*(11), 783–786. https://doi.org/10.1038/ngeo1269

Hsu, Y.-J., Simons, M., Yu, S.-B., Kuo, L.-C., & Chen, H.-Y. (2003). A two-dimensional dislocation model for interseismic deformation of the Taiwan mountain belt. *Earth and Planetary Science Letters*, *211*(3), 287–294. https://doi.org/10.1016/S0012-821X(03)00203-6

Inbal, A., Ampuero, J.-P., & Avouac, J.-P. (2017). Locally and remotely triggered aseismic slip on the central San Jacinto fault near Anza, CA, from joint inversion of seismicity and strainmeter data. *Journal of Geophysical Research: Solid Earth*, *122*, 3033–3061. https://doi.org/10.1002/2016JB013499

Jónsson, S., Zebker, H., Cervelli, P., Segall, P., Garbeil, H., Mouginis-Mark, P., & Rowland, S. (1999). A shallow-dipping dike fed the 1995 flank eruption at Fernandina volcano, Galapagos, observed by satellite radar interferometry. *Geophysical Research Letters*, *26*(8), 1077–1080. https://doi.org/10.1029/1999GL900108

Key, J., White, R. S., Soosalu, H., & Jakobsdóttir, S. S. (2011). Multiple melt injection along a spreading segment at Askja, Iceland. *Geophysical Research Letters*, *38*, L05301. https://doi.org/10.1029/2010GL046264

LaFemina, P. C., Dixon, T. H., Malservisi, R., Árnadóttir, Þ., Sturkell, E., Sigmundsson, F., & Einarsson, P. (2005). Geodetic GPS measurements in south Iceland: Strain accumulation and partitioning in a propagating ridge system. *Journal of Geophysical Research*, *110*, B11405. https://doi.org/10.1029/2005JB003675

Larsen, G., & Grönvold, K. (1979). Volcanic eruption through a geothermal borehole at Namafjall, Iceland. *Nature*, *278*, 707–710.

Linker, M. F., & Dieterich, J. H. (1992). Effects of variable normal stress on rock friction: Observations and constitutive equations. *Journal of Geophysical Research*, *97*(B4), 4923–4940. https://doi.org/10.1029/92JB00017

Marsan, D., & Lengline, O. (2008). Extending earthquakes' reach through cascading. *Science*, *319*(5866), 1076–1079. https://doi.org/10.1126/science.1148783

Parks, M. M., Heimisson, E. R., Sigmundsson, F., Hooper, A., Vogfjörd, K. S., Árnadóttir, Þ., et al. (2017). Evolution of deformation and stress changes during the caldera collapse and dyking at Bárdarbunga, 2014–2015: Implication for triggering of seismicity at nearby Tungnafellsjökull volcano. *Earth and Planetary Science Letters*, *462*, 212–223. https://doi.org/10.1016/j.epsl.2017.01.020

Rubin, A. M. (1993). Tensile fracture of rock at high confining pressure: Implications for dike propagation. *Journal of Geophysical Research*, *98*(B9), 15,919–15,935. https://doi.org/10.1029/93JB01391

Rubin, A. M., & Gillard, D. (1998). Dike-induced earthquakes: Theoretical considerations. *Journal of Geophysical Research*, *103*(B5), 10,017–10,030. https://doi.org/10.1029/97JB03514

Ruch, J., Wang, T., Xu, W., Hensch, M., & Jónsson, S. (2016). Oblique rift opening revealed by reoccurring magma injection in central Iceland. *Nature communications*, *7*, 12352. https://doi.org/10.1038/ncomms12352

Savage, J. C., & Burford, R. O. (1973). Geodetic determination of relative plate motion in central California. *Journal of Geophysical Research*, *78*(5), 832–845. https://doi.org/10.1029/JB078i005p00832

Segall, P., Llenos, A. L., Yun, S.-H., Bradley, A. M., & Syracuse, E. M. (2013). Time-dependent dike propagation from joint inversion of seismicity and deformation data. *Journal of Geophysical Research: Solid Earth*, *118*, 5785–5804. https://doi.org/10.1002/2013JB010251

Sigmundsson, F., Hooper, A., Hreinsdottir, S., Vogfjörð, K. S., Ófeigsson, B. G., Heimisson, E. R., et al. (2015). Segmented lateral dyke growth in a rifting event at Bardarbunga volcanic system, Iceland. *Nature*, *517*(7533), 191–195. https://doi.org/10.1038/nature14111

Sigmundsson, F., Hreinsdóttir, S., Hooper, A., Árnadóttir, Þ., Pedersen, R., Roberts, M. J., et al. (2010). Intrusion triggering of the 2010 Eyjafjallajokull explosive eruption. *Nature*, *468*(7322), 426–430. https://doi.org/10.1038/nature09558

Soosalu, H., Key, J., White, R., Knox, C., Einarsson, P., & Jakobsdóttir, S. S. (2010). Lower-crustal earthquakes caused by magma movement beneath Askja volcano on the north Iceland rift. *Bulletin of Volcanology*, *72*(1), 55–62. https://doi.org/10.1007/s00445-009-0297-3

Spaans, K., & Hooper, A. (2018). Insights into the stress field around Bárdarbunga volcano from the 2014/2015 Holuhraun rifting event. *Journal of Geophysical Research: Solid Earth*, *123*, 3238–3249. https://doi.org/10.1002/2017JB015274

Sparks, R., Meyer, P., & Sigurdsson, H. (1980). Density variation amongst mid-ocean ridge basalts: Implications for magma mixing and the scarcity of primitive lavas. *Earth and Planetary Science Letters*, *46*(3), 419–430.

Sturkell, E., & Sigmundsson, F. (2000). Continuous deflation of the Askja caldera, Iceland, during the 1983–1998 noneruptive period. *Journal of Geophysical Research*, *105*(B11), 25,671–25,684. https://doi.org/10.1029/2000JB900178

Townsend, M. R., Pollard, D. D., & Smith, R. P. (2017). Mechanical models for dikes: A third school of thought. *Tectonophysics*, *703–704*, 98–118. https://doi.org/10.1016/j.tecto.2017.03.008

Yun, S., Segall, P., & Zebker, H. (2006). Constraints on magma chamber geometry at Sierra Negra Volcano, Galapagos Islands, based on InSAR observations. *Journal of Volcanology and Geothermal Research*, *150*(1), 232–243. https://doi.org/10.1016/j.jvolgeores.2005.07.009, the Changing Shapes of Active Volcanoes.